

Object Sensing and Shape Detection Using Vibrissa Hair-like Sensors with Intrinsic Curvature

Carsten Behn*, Christoph Will*, Anton Sauter*, Tobias Preiß* and Joachim Steigenberger†

*Department of Mechanical Engineering

†Institute of Mathematics

Technische Universität Ilmenau, Ilmenau, Germany, 98693

Email: {carsten.behn, christoph.will, anton.sauter, tobias.preiss, j.steigenberger}@tu-ilmenau.de

Abstract—Numerous mammals possess in addition to normal body hairs tactile hairs, also known as vibrissae or whiskers, to explore their environment. Biological observations have shown that rodents use their tactile hairs in the snout region (mystacial vibrissae) to estimate obstacle contact and obstacle shape within a few contacts of the tactile hair. Despite different morphology of animal vibrissae (e.g., cylindrically or conically shaped, pre-curved, multi-layer structure), these biological tactile hairs are modeled in a mechanical way to develop and analyze models concerning their bending behavior with a glance to get hints for a technical implementation as a technical sensor. We focus on an analytical description, numerical simulations and experimental verifications of an object scanning process to achieve a better understanding of this sense. We investigate the bending behavior of cylindrically shaped rods with an intrinsic curvature, which are one-sided clamped and interact with a rigid obstacle in the plane. Hence, the sensing element vibrissa is under the load of an external contact force during object scanning and is frequently modeled as an Euler-Bernoulli bending rod allowing for large deflections. Most of the literature is limited to the research on cylindrical & straight, or tapered & straight rods. The (natural) intrinsic curved shape is rarely analyzed. Hence, the aim is to determine the obstacles contour by one quasi-static sweep along the obstacle and to figure out the dependence on the intrinsic curvature of the rod. The consideration of an intrinsic curvature makes the analytical treatment a bit harder and results in numerical solutions of the process. Nevertheless, at first, we focus on a constant intrinsic curvature and, then, present simulations and experiments using a variable one.

Keywords—Vibrissa; intrinsic curvature; sensing; object scanning; contour reconstruction.

I. INTRODUCTION

In recent years, the design and development of vibrissae-inspired tactile sensors gain center stage in the focus of research. This paper contributes to these investigations of intelligent tactile sensors and extends the results of [1]. There is a great interest in tactile sensors, especially in the field of (autonomous) robotics, see e.g., [2]–[8], since these tactile sensors complement to and/or replace senses like vision, because they provide reliable information in a dark and noisy environment (e.g., seals detect freshet and turbulence of fish in muddy water [9]–[11]), and are cheaper in fabrication.

A. Motivation from Biology

In many technical developments, engineers often use biological systems as an inspiration. A tactile sensor system, which attracted attention in recent years, is the so-called *sinus*

hair. This tactile sensory organ with incomparable abilities can be found on the body of mammals. Despite existing differences regarding musculature and localization, they are synonymously also known as *vibrissae* or *whiskers* [12]. Depending on their localization on the body they are used for several tasks like

- object recognition [13],
- object discrimination [10] [14], and
- perception of flow [10] [15], as well as
- for social behavior [16].

Sinus hairs differ from typical body hairs:

- they are thicker, longer and stiffer than body hairs [17],
- each sinus hair is supported/embedded in its own follicle-sinus complex (FSC), that is characterized by its exceptional arrangement of blood vessels, neural connections and muscles [18],
- they are made of dead material, i.e., the hair shaft itself has no receptors along its length [19], hence they are mainly used for the transmission for all tactile stimuli arising along the shaft, and
- they feature an intrinsic curvature, a conical shape, cylindrical cross-section and are made of different material with hollow parts (like a multi-layer system) [17] [20] [21].

As mentioned, rodents use their sinus hairs to acquire information about their surroundings. The movement and deformation of the vibrissa due to contacts to several objects can only be detected by mechanoreceptors in the FSC [2] [22]. Hence, the animal draws its conclusions about the environment only from these (measured) quantities at the base of the hair – the support reactions. We do not want to explain the transmission of mechanical stimuli during object contact to the mechanoreceptors in the follicle, rather we want to analyze the influence of the geometrical properties of a sinus hairs on these support reactions, which are used for object recognition and contour reconstruction.

B. Goal

In this paper, the investigations focus the influence of the *intrinsic curvature* to the bending behavior of a vibrissa due to an obstacle contact during object sensing. This intrinsic curvature is due to a kind of protection role: purely axial forces

are prevented and, including the conical shape, the area of the tip of the vibrissa is limp. This results in a tangential contact to an object [20] [23]. We describe a quasi-static scanning process of obstacles: 1. analytical/numerical generation of the observables in the support, which an animal solely relies on, 2. reconstruction of the scanned profile contour using only these observables, and 3. verification of the working principle by means of experiments. These steps were done in [8], [24] and [25] for cylindrical vibrissae. In [1], the influence of a *constant* intrinsic curvature was investigated, here, we extend these results to rods with a *variable* intrinsic curvature in this paper.

C. Arrangement

The paper is arranged as follows: We give a short overview on the related literature in Section II, which is quite rare and often starts up with some approximations of the problem. Section III is devoted to the governing equations describing an Euler-Bernoulli rod with intrinsic curvature under large deflections – nonlinear theory. In Section IV, we present the scanning process, which has to be divided into two phases: tip contact of the rod with the object, or tangential contact within the rod's length. For this, we set up two mechanical models to describe these scenarios – ordinary differential equations with boundary- or initial- condition. These equations are exemplarily solved in Section V – considering firstly a constant intrinsic curvature radius of the bending rod, and then a variable one. The results are performed to test the reconstruction algorithm to detect the obstacle's boundary. The effectiveness of the algorithm is then verified by experiments in Section VI using three different artificial vibrissae. Then, the paper closes in Section VII with a conclusion and an outlook on future work.

II. SOME STATE OF ART OF MODELING VIBRISSAE WITH INTRINSIC CURVATURE

From the biological point of view, there are a lot of works focussing on the determination of vibrissae parameters. Towal et al. [21] pointed out an important fact that the mostly vibrissae are curved in a plane. The deviation of the vibrissa from this plane (referred to the length) is less than 0.1%. In [21], [23] and [26]–[30], a vibrissa is described using a polynomial approximation of 2nd-, 3rd- and 5th-order, which is rather low. In contrast to this references, we present numerical results using one of order 10. In [23], it is stated that approximately 90% of rat vibrissae exhibit an intrinsic curvature $\kappa_0 \in (0.0065/mm, 0.074/mm)$, and in [28] that extremely curved vibrissa provide $\kappa_0 > 0.25/mm$. The authors of [17], [23], [28] publish the following dimensionless parameters

$$\frac{L}{d} \approx 30, \quad \frac{r_0}{d} \approx 90,$$

whereas L is the length, d is the base diameter, and r_0 is the intrinsic curvature radius of the vibrissa.

From the technical point of view, pre-curved vibrissae are rarely used in applications. In [23], [29], [30], experimental and theoretical investigations concerning the distance detection to a pole are presented, using a pre-curved artificial vibrissa, also incorporating the conical shape. The pros and cons of a positive (curvature forward, CF) and negative (CB) curved vibrissae are stated in [23] whereas the vibrissa is used for

tactile sensing of a pole. The CF-scanning results in low axial forces, but higher shear ones; CB the inverse results. Summarized, the pre-curvature influences mainly the support forces instead of the support moment.

III. MODELING

The deflection of a largely deformed rod with intrinsic curvature is described in using the so-called *Winkler-Bach-Theory*. A detailed derivation of the equations can be found in [32].

At first, we derive the equations of stress and deformation of the rod – using an infinitesimal small element of a rod with intrinsic curvature, presented in Figures 1–3, whereas we have the following relation between curvature κ and curvature radius r :

$$\kappa_0(s) = \frac{1}{r_0(s)} \quad (1)$$

$$\kappa(s) = \frac{1}{r(s)} \quad (2)$$

whereas the index “0” means undeformed state.

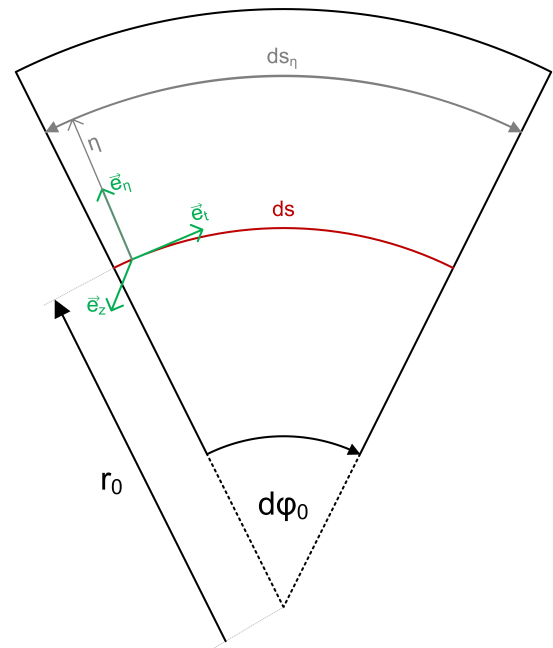


Figure 1. Initial state of no load.

$$d\varphi = d\varphi_0 + d\psi$$

The strain of the rod axis is

$$\varepsilon(s, \eta = 0) = \frac{du(s, \eta = 0)}{ds} \quad (3)$$

The length of a fiber in distance η to the rod axis is

$$ds_\eta(s, \eta) = (r_0(s) - \eta) \cdot d\varphi_0. \quad (4)$$

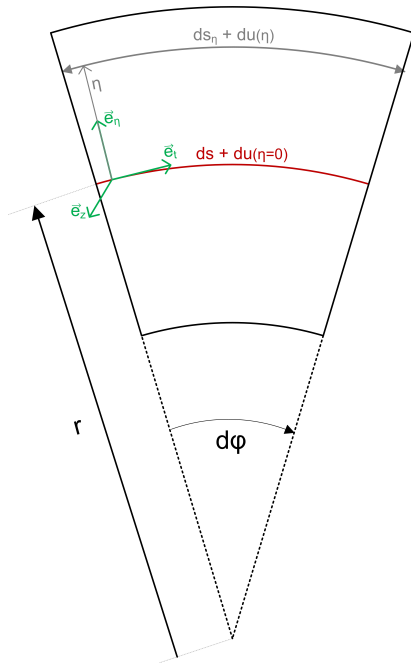


Figure 2. Deformed state of an infinitesimal rod element.

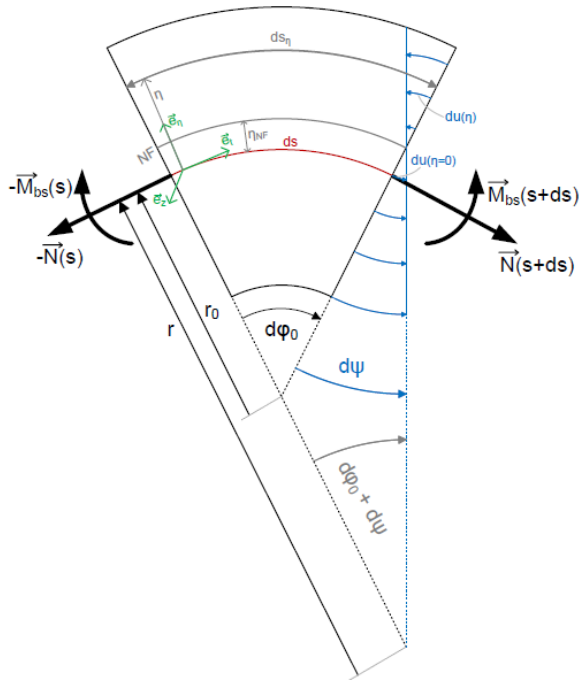


Figure 3. Rod element with stress resultants.

Hence, we get

$$\varepsilon(s, \eta) = \frac{du(s, \eta)}{ds_\eta(s, \eta)} = \frac{du(s, \eta=0) - \eta \cdot d\psi}{(r_0(s) - \eta) \cdot d\varphi_0} \quad (5)$$

$$= \frac{\varepsilon(s, \eta=0) \cdot r_0(s) \cdot d\varphi_0 - \eta \cdot d\psi}{(r_0(s) - \eta) \cdot d\varphi_0} \quad (6)$$

$$\rightarrow \varepsilon(s, \eta) = \varepsilon(s, \eta=0) + \left(\varepsilon(s, \eta=0) - \frac{d\psi}{d\varphi_0} \right) \frac{\eta}{r_0 - \eta} \quad (7)$$

To determine $\varepsilon(s, \eta = 0)$ and $\frac{d\psi}{d\varphi_0}$ we introduce the stress resultants bending moment $\vec{M}_{bs}(s)$ and normal force $\vec{N}(s)$. Applying Hooke's law of elasticity (8)

$$\sigma(s, \eta) = E \cdot \varepsilon(s, \eta) \quad (8)$$

we get

$$N(s) = \int_A \sigma(s, \eta) dA = E \cdot \left(\varepsilon(s, \eta=0) \cdot A + \left(\varepsilon(s, \eta=0) - \frac{d\psi}{d\varphi_0} \right) \cdot \int_A \frac{\eta}{r_0(s) - \eta} dA \right) \quad (9)$$

$$M_{bs}(s) = - \int_A \sigma(s, \eta) \cdot \eta dA = -E \cdot \left(\varepsilon(s, \eta=0) \cdot \underbrace{\int_A \eta dA}_0 + \left(\varepsilon(s, \eta=0) - \frac{d\psi}{d\varphi_0} \right) \cdot \int_A \frac{\eta^2}{r_0(s) - \eta} dA \right) \quad (10)$$

Introducing the following parameter, see [32],

$$\lambda(s) := \frac{1}{A} \int_A \frac{\eta}{r_0(s) - \eta} dA \quad (11)$$

yields:

$$\varepsilon(s, \eta=0) - \frac{d\psi}{d\varphi_0} = \frac{-M_{bs}(s)}{\lambda(s) \cdot r_0(s) \cdot E \cdot A} \quad (12)$$

$$\varepsilon(s, \eta=0) = \frac{1}{E \cdot A} \cdot \left(N(s) + \frac{M_{bs}(s)}{r_0(s)} \right) \quad (13)$$

Substituting (13) and (12) in (7) yields the equation of the stress:

$$\sigma(s, \eta) = \frac{N(s)}{A} + \frac{M_{bs}(s)}{A r_0(s)} \cdot \left(1 - \frac{1}{\lambda(s)} \cdot \frac{\eta}{r_0(s) - \eta} \right) \quad (14)$$

The determination of the equation of deformation is based on the consideration of the deformation of the rod axis ($\eta = 0$), having a glance to Figure 3:

$$ds + du(s, \eta = 0) = r(s) \cdot (d\varphi_0 + d\psi) \quad (15)$$

Using

$$du(s, \eta = 0) = ds \cdot \varepsilon(s, \eta = 0) \quad \text{and} \quad ds = r_0(s) \cdot d\varphi_0$$

we get:

$$r_0(s) \cdot \left(1 + \varepsilon(s, \eta = 0) \right) = r(s) \cdot \left(1 + \frac{d\psi}{d\varphi_0} \right) \quad (16)$$

Replacing $\frac{d\psi}{d\varphi_0}$ by (12) yields:

$$r_0(s) \cdot \left(1 + \varepsilon(s, \eta = 0) \right) = r(s) \cdot \left(1 + \frac{M_{bs}(s)}{\lambda(s) \cdot r_0(s) \cdot E \cdot A} + \varepsilon(s, \eta = 0) \right) \quad (17)$$

The arising formula for the curvature κ is:

$$\begin{aligned}\kappa(s) &= \frac{1}{r(s)} \\ &= \frac{1}{r_0(s)} \cdot \left(1 + \frac{M_{bs}(s)}{\lambda(s) \cdot r_0(s) \cdot E \cdot A} \cdot \frac{1}{1 + \varepsilon(s, \eta = 0)} \right)\end{aligned}\quad (18)$$

Now, replacing $\varepsilon(s, \eta = 0)$ by (13), there arises a formula for the curvature $\kappa(s)$ (after deformation) or the curvature radius $r(s)$, respectively:

$$\begin{aligned}\kappa(s) = \frac{1}{r(s)} &= \frac{1}{r_0(s)} + \frac{M_{bs}(s)}{\lambda(s)r_0(s)^2EA} \\ &\cdot \frac{1}{1 + \frac{1}{EA} \cdot \left(N(s) + \frac{M_{bs}(s)}{r_0(s)} \right)}\end{aligned}\quad (19)$$

Having a glance to Figure 2 it is obvious:

$$ds \left(1 + \varepsilon(s, \eta = 0) \right) = r \cdot d\varphi \quad (20)$$

$$\frac{d\varphi}{ds} = \frac{1}{r(s)} \left(1 + \varepsilon(s, \eta = 0) \right) \quad (21)$$

Applying (18) we get:

$$\frac{d\varphi(s)}{ds} = \frac{1}{r_0(s)} \cdot \left(1 + \varepsilon(s, \eta = 0) + \frac{M_{bs}(s)}{\lambda(s) \cdot r_0(s) \cdot E \cdot A} \right)$$

Finally, using (13) there is the equation of deformation:

$$\boxed{\frac{d\varphi(s)}{ds} = \frac{1}{r_0(s)} \cdot \left(1 + \frac{N(s)}{EA} + \frac{M_{bs}(s)}{EA r_0(s)} \cdot \left(1 + \frac{1}{\lambda(s)} \right) \right)} \quad (22)$$

Considering the special case, that the radius of intrinsic curvature is much greater than the dimensions of the cross-section, then the influence of the normal force can be neglected [33]. Hence, the describing equations can be simplified to

$$\frac{d\varphi(s)}{ds} = \frac{1}{r_0(s)} + \frac{M_{bs}(s)}{E I_z}, \quad (23)$$

with second moment of area

$$I_z := \int_{(A)} \eta^2 dA,$$

and Young's modulus E , cross-section A , bending moment M_{bs} , and radius of pre-curvature r_0 .

IV. SCANNING PROCEDURE

Here, we describe the scanning procedure of *strictly convex profile contours* using pre-curved technical vibrissae *in a plane*. This is done in two steps:

1. Because of analytical interest, we firstly generate the observables (support reactions) during the scanning process. Since our intension is from bionics, we simply model the support as a clamping (being aware that this does not match the reality). Hence, the support

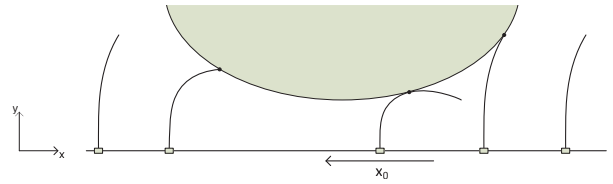


Figure 4. Scanning procedure using an artificial vibrissa; adapted from [8].

reactions are the clamping forces and moment \vec{M}_{Az} , \vec{F}_{Ax} , \vec{F}_{Ay} , which an animal solely relies on.

2. Then, we use these observables in an algorithm to reconstruct the profile contour.

Figure 4 sketches the scanning process of a plane, strictly profile. For this scanning process, several assumptions are made:

- The technical vibrissa is moved from *right to the left* (negative x -direction), i.e., the base point is moved.
- The problem is handled *quasi-statically*, i.e., the vibrissa is moved incrementally (and presented in changes of the boundary conditions). Then, the elastically deformed vibrissa is determined.
- Since we do not want to deal with friction at the beginning, we assume an *ideal contact*, i.e., the contact force is *perpendicular* to the contact point tangent of the profile.

The scanned profile is given by a function $g : x \mapsto g(x)$, where $g \in C^1(\mathbb{R}; \mathbb{R})$. Since the graph of g is convex by assumption, the graph can be parameterized by means of the slope angle α in the xy -plane. Then we have, [8]:

$$\begin{aligned}\frac{dg(x)}{dx} &= g'(x) = \tan(\alpha) \\ \xrightarrow{x} &= \xi(\alpha) := g'^{-1}(\tan(\alpha)) \\ y &= \eta(\alpha) := g(\xi(\alpha))\end{aligned}$$

Therefore, each point of the profile contour is given by $(\xi(\alpha), \eta(\alpha))$, $\alpha \in (-\frac{\pi}{2}; \frac{\pi}{2})$. For generality, we introduce dimensionless variables, starting with the arc length s with $s = Ls^*$, $s^* \in [0, 1]$. Then, the basic units are:

$$[length] = \mathbf{L}, \quad [moment] = \frac{\mathbf{E}\mathbf{I}_z}{\mathbf{L}}, \quad [force] = \frac{\mathbf{E}\mathbf{I}_z}{\mathbf{L}^2}$$

Remark IV.1. For the sake of brevity, we omit the asterisk "*" from now on.

A. Boundary-value Problem in Step 1

The system of differential equations (ODEs) describing the deformed pre-curved, technical vibrissa in a plane in dimensionless quantities is:

$$\left. \begin{aligned}\frac{dx(s)}{ds} &= \cos(\varphi(s)) \\ \frac{dy(s)}{ds} &= \sin(\varphi(s)) \\ \frac{d\varphi(s)}{ds} &= \frac{1}{r_{0L}(s)} + f\left(\left(y(s) - \eta(\alpha)\right) \sin(\alpha) \right. \\ &\quad \left. + \left(x(s) - \xi(\alpha)\right) \cos(\alpha)\right)\end{aligned}\right\} \quad (24)$$

Observing Figures 4 and 5 gives the hint to distinguish two phases of contact between the vibrissa and the obstacle:

- **Phase A – tip contact:** We have still ODE-system (24) with the boundary conditions (BCs)

$$\begin{aligned} y(0) &= 0, & \varphi(0) &= \frac{\pi}{2}, \\ x(1) &= \xi(\alpha), & y(1) &= \eta(\alpha) \end{aligned} \quad (25)$$

- **Phase B – tangential contact:** Only the BCs change:

$$\begin{aligned} y(0) &= 0, & \varphi(0) &= \frac{\pi}{2}, \\ x(s_1) &= \xi(\alpha), & y(s_1) &= \eta(\alpha), & \varphi(s_1) &= \alpha \end{aligned} \quad (26)$$

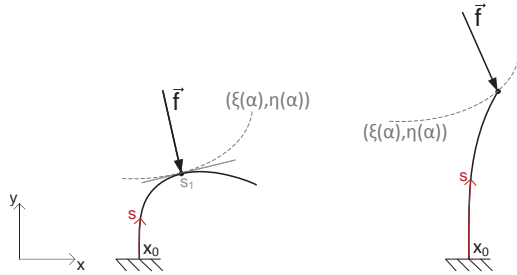


Figure 5. Contact of vibrissa and obstacle in Phase A (left) and in Phase B (right) during scanning process.

A direct inspection of the occurring problems (24)&(25) and (24)&(26) yield the choice of a shooting method to determine the parameters f and s_1 , and finally with f the clamping reactions \vec{M}_{Az} , \vec{F}_{Ax} , \vec{F}_{Ay} .

B. Initial-value Problem in Step 2

Here, we use only the generated observables (measured in experiments) \vec{M}_{Az} , \vec{F}_{Ax} , \vec{F}_{Ay} and known base of the vibrissa x_0 to reconstruct the scanned profile. Due to [31], we determine the bending moment, see Figure 6, to formulate the initial-value problem (IVP) in this step:

$$\left. \begin{aligned} \frac{dx(s)}{ds} &= \cos(\varphi(s)) \\ \frac{dy(s)}{ds} &= \sin(\varphi(s)) \\ \frac{d\varphi(s)}{ds} &= \frac{1}{r_{0L}(s)} - M_{Az} - F_{Ax}y(s) + F_{Ay}(x(s) - x_0) \end{aligned} \right\} \quad (27)$$

with initial conditions (ICs)

$$x(0) = x_0, \quad y(0) = 0, \quad \varphi(0) = \frac{\pi}{2} \quad (28)$$

Now, it is necessary – for each input $\{M_{Az}, F_{Ax}, F_{Ay}, x_0\}$ – to determine the contact point $(x(s_1), y(s_1))$ (note, that s_1 is known in step 1, but is not an observable). But, it is still unknown, in which phase we are. We only have

$$M_{bz}(s_1) = 0$$

In accordance to [8], we determine a decision criterion to distinguish both phase. The vibrissa is in Phase B, if and only

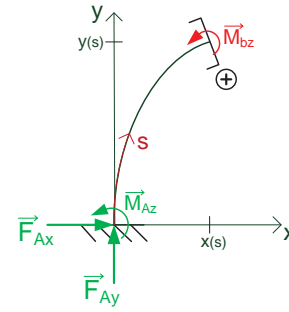


Figure 6. Applying method of sections to the vibrissa.

if it holds:

$$M_{Az}^2 + \frac{2M_{Az}}{r_{0L}} - 2F_{Ay} = 0 \quad (29)$$

In comparison to the condition in [8], we get one new term $\frac{2M_{Az}}{r_{0L}}$. And, in a limiting case for $r_{0L} \rightarrow \pm\infty$, condition (29) forms the condition in [8], which serves as a validation.

V. SIMULATIONS OF PROFILE SCANNING

Referring to [8], we consider a profile described by

$$g_1 : x \mapsto \frac{1}{2}x^2 + 0.3. \quad (30)$$

A. Scanning Using a Constant Intrinsic Curvature Radius

Here, we present numerical simulations of the described profile scanning algorithm (based of two steps). At first, we focus on a *constant* pre-curvature radius $r_{0L} \neq r_{0L}(s)$.

Exemplarily, the scanning process is performed for several values of r_{0L} and the results are presented in Figures 7–10.

Remark V.1. Note, that the vibrissae in Phase B are only plotted to the contact point, just for clarity.

One can clearly see, that the smaller the pre-curvature radius is no Phase A occurs, i.e., no tip contact, which might explain the protective role of the pre-curvature of vibrissae.

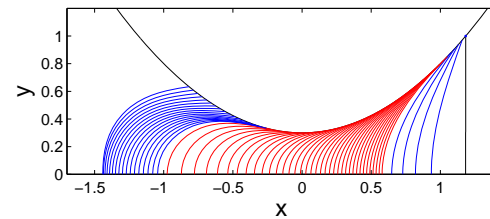


Figure 7. Profile scanning using a pre-curved vibrissa with $r_{0L} = -1000$: in blue Phase A, in red Phase B.

Figures 11–13 show the observables during a scanning process in dependence on the pre-curvature radius. The transition between both phases is marked with a “+”. It becomes clear: the smaller the pre-curvature radius the smaller the bending behavior of the vibrissa, the smaller the observables, but the smaller the scanning area. Therefore, a small pre-curvature radius results in poor scanning results.

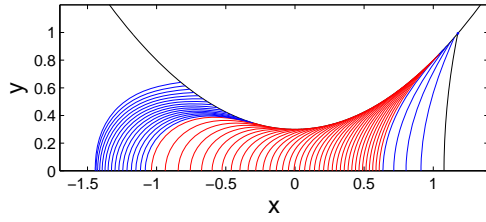


Figure 8. Profile scanning using a pre-curved vibrissa with $r_{0L} = -5$: in blue Phase A, in red Phase B.

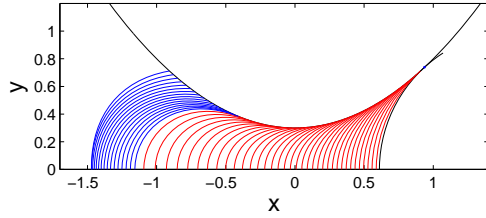


Figure 9. Profile scanning using a pre-curved vibrissa with $r_{0L} = -1$: in blue Phase A, in red Phase B.

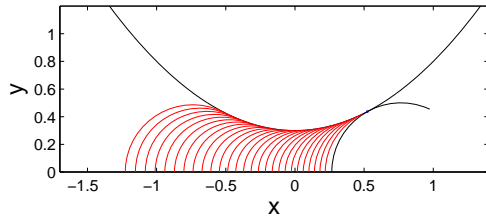


Figure 10. Profile scanning using a pre-curved vibrissa with $r_{0L} = -0.5$: in red Phase B, no Phase A.

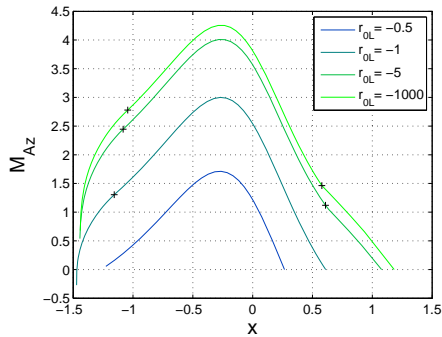


Figure 11. Clamping moment M_{Az} for varying pre-curvature radius r_{0L} .

The error of the reconstruction between the given and reconstructed profile is defined for single points according to [8]:

$$error = \sqrt{(x_k(s_{1k}) - \xi(\alpha_k))^2 + (y_k(s_{1k}) - \eta(\alpha_k))^2}, \quad (31)$$

whereby $(\xi(\alpha_k), \eta(\alpha_k))$ represent a point of the given profile and $(x_k(s_{1k}), y_k(s_{1k}))$ is the corresponding one of the recon-

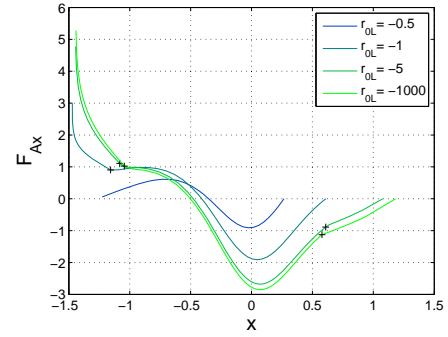


Figure 12. Clamping force F_{Ax} for varying pre-curvature radius r_{0L} .

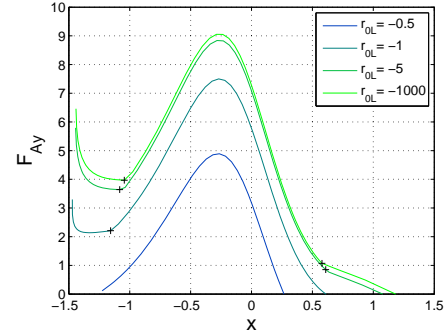


Figure 13. Clamping force F_{Ay} for varying pre-curvature radius r_{0L} .

structed profile. Figures 14–17 present the reconstruction errors of the simulations. The magnitude of the error is from 10^{-7} to 10^{-6} , which is quite good.

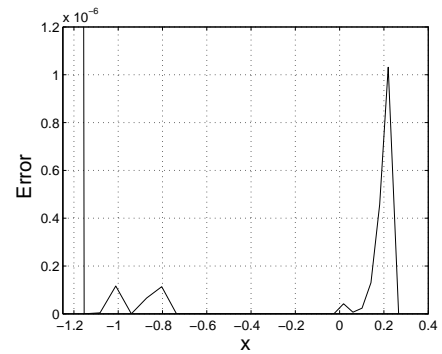


Figure 14. Error of given and reconstructed profile for $r_{0L} = -0.5$.

B. Scanning Using a Variable Intrinsic Curvature Radius

In this subsection, the parabola profile from (30) is scanned and reconstructed in using an artificial tactile rod with a variable intrinsic curvature of the form:

$$r_{0L}(s) = -5 + 4.2 \cdot s^{\frac{1}{3}}, \quad s \in [0, 1] \quad (32)$$

The scanning process is presented in Figure 18, the clamping reactions are displayed in Figure 19, and the reconstruction error is shown in Figure 20.

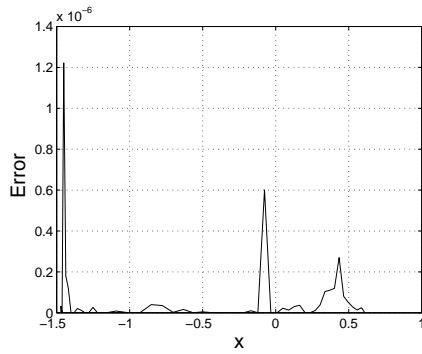


Figure 15. Error of given and reconstructed profile for $r_{0L} = -1$.

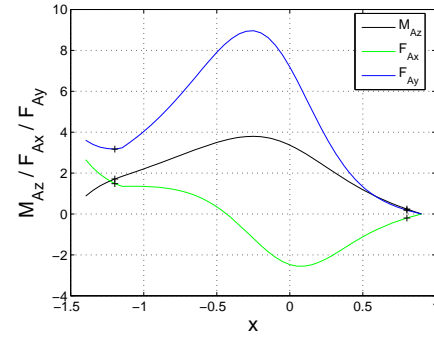


Figure 19. Clamping reactions varying pre-curvature radius $r_{0L}(s)$ of (32).

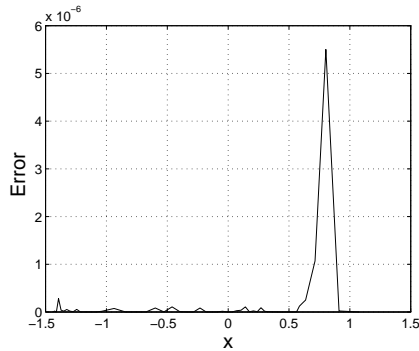


Figure 16. Error of given and reconstructed profile for $r_{0L} = -5$.

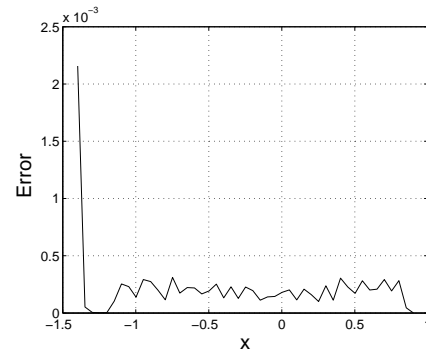


Figure 20. Error of given and reconstructed profile for $r_{0L}(s)$ of (32).

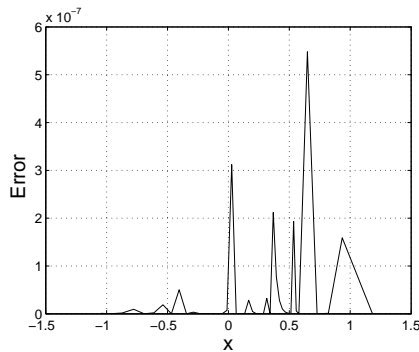


Figure 17. Error of given and reconstructed profile for $r_{0L} = -1000$.

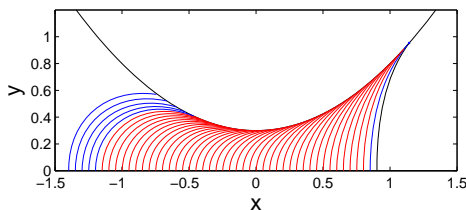


Figure 18. Profile scanning using a pre-curved vibrissa with $r_{0L}(s)$ of (32): in red Phase B, no Phase A.

Comparing these results in using a rod with variable intrinsic curvature with the results using a straight cylindrical rod, i.e., r_{0L} is very high like $r_{0L} = 1000$ (see Figures 7,

11–13), than we can increase the scanned area of the profile whereas the clamping reactions still stay at their values. It is not really desirable to diminish the values of the clamping reaction because of possible measurement problems.

The numerical simulation of scanning object contours using artificial sinus hair-like tactile sensors of both constant and variable intrinsic curvature work very well. Therefore, we go on to the next step: experimental verification in the next section.

VI. EXPERIMENTS

To verify the algorithms, we present numerical investigations of scanning vibrissae with variable intrinsic curvature and experimental results, using the parabola profile

$$x \mapsto g_1(x) = 2x^2 + 0.55.$$

Three different technical vibrissae with different pre-curvature are used in an experiment. Figure 21 shows that the first vibrissa is a straight one, the second and the third one have a variable intrinsic curvature radius.

With the help of a computer-aided evaluation of the graphic representation of the vibrissae in Figure 21, their intrinsic curvature radius $r_{0L}(s)$ is determined in dependence on the arc length s as polynomials of order 10. This is rather new in literature, because a lot of works from literature restrict to a representation of the pre-curvature only to s^2 -terms.

The simulated scanning processes are shown in Figures 23 and 24 for vibrissa 1 and 3.

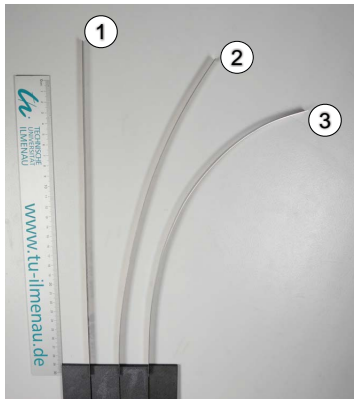


Figure 21. Three different pre-curved vibrissae for the experiment.

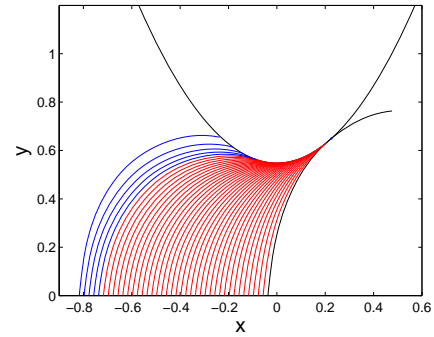


Figure 24. Scanning process using vibrissa 3 – in blue *Phase A*; in red *Phase B*.

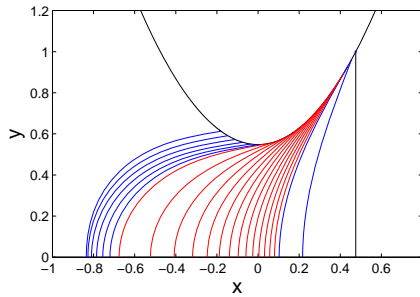


Figure 22. Scanning process using vibrissa 1 – in blue *Phase A*; in red *Phase B*.

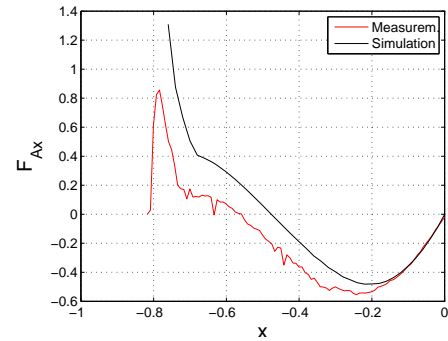


Figure 25. Experiment using vibrissa 3: clamping force F_{Ax} of a simulation and the experiment.

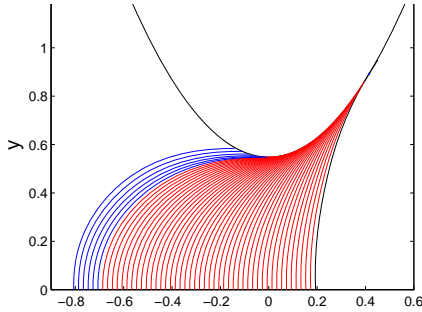


Figure 23. Scanning process using vibrissa 2 – in blue *Phase A*; in red *Phase B*.

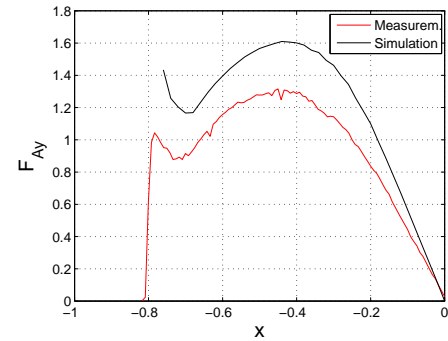


Figure 26. Experiment using vibrissa 3: clamping force F_{Ay} of a simulation and the experiment.

Figures 25–27 show exemplarily the observables (simulation vs. experiment) of the experiment using vibrissa 3. An easy inspection confirms prior results, that the maximal values of M_{Az} , F_{Ax} and F_{Ay} decrease the bigger the intrinsic curvature and the smaller the intrinsic curvature radius are. These figures show a good coincidence of the simulated and measured curves of the observables.

Summarizing, the following Figures 28–30 present the reconstruction of the profile. Compared to further simulations, we point out that the smaller the intrinsic curvature radius is the smaller is the reconstruction error. Finally, we conclude that it is promising to use pre-curved vibrissae for object contour scanning and reconstruction. The simulated and measured curves of the observables show up a good coincidence. The presented algorithms work effectively.

VII. CONCLUSION

Due to the functionality of animals vibrissae, the goal was to set up a model for an object scanning and shape reconstruction algorithm. For this, the only available information are the observables (support reaction, which an animal solely relies on) governed by one single sweep along the profile. Based on these observables, the object boundary has to be reconstructed.

It was possible to illustrate the characteristics and influences of pre-curved technical vibrissae in view of profile scanning. Based on the Winkler-Bach-Theory for pre-curved beams we set up the equations for a deformed vibrissa during a scanning process. We presented an algorithm to reconstruct the scanned profile in using the generated observables (which an

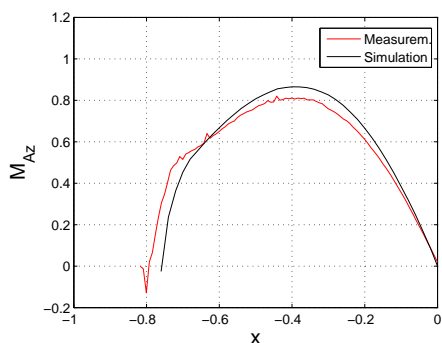


Figure 27. Experiment using vibrissa 3: clamping moment M_{Az} of a simulation and the experiment.

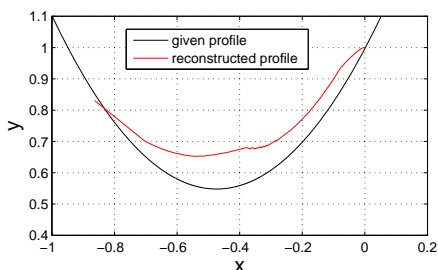


Figure 28. Given and reconstructed profile using vibrissa 1.

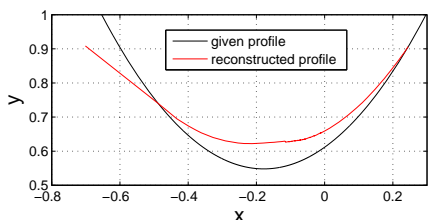


Figure 29. Given and reconstructed profile using vibrissa 2.

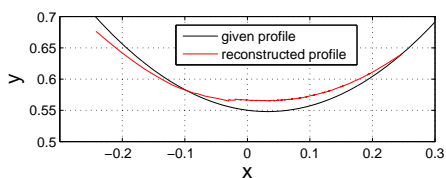


Figure 30. Given and reconstructed profile using vibrissa 3.

animal is supposed to solely rely on) via shooting methods. The reconstruction then was based on solving initial-value problems on contrast to the generation procedure where we

solved boundary-value problems. The investigations respective the scanning of a strictly convex profile with a pre-curved vibrissae showed noticeable differences to the profile scanning with a straight vibrissa. The extrema of the bending reactions and the size of the scanned profile area depends on the pre-curvature radius of the vibrissa. Using a smaller radius, the tangential contact *phase B* in the scanning process could be enlarged. Experiments confirmed the numerical results and algorithms in this paper. Moreover, the investigation showed that the profile reconstruction works better with a pre-curved vibrissa.

REFERENCES

- [1] C. Behn, J. Steigenberger, A. Sauter, and C. Will, "Pre-curved Beams as Technical Tactile Sensors for Object Shape Recognition," in *Proceedings INTELLI 2016: The Fifth International Conference on Intelligent Systems and Applications*, Barcelona (Spain), November 2016, IARIA, ISBN: 978-1-61208-518-0, pp. 7–12, 2016.
- [2] R. Berg and D. Kleinfeld, "Rhythmic Whisking by Rat: Retraction as Well as Protraction of the Vibrissae Is Under Active Muscular Control," *Journal of Neurophysiology*, vol. 89, no. 1, pp. 104–117, 2002.
- [3] G.R. Scholz and C.D. Rahn, "Profile Sensing With an Actuated Whisker," *IEEE Transactions on Robotics and Automation*, vol. 20, no. 1, pp. 124–127, 2004.
- [4] M.J. Pearson et al., "A Biologically Inspired Haptic Sensor Array for use in Mobile Robotic Vehicles," in *Proceedings of Towards Autonomous Robotic Systems (TAROS)*, pp. 189–196, 2005.
- [5] M.J. Pearson et al., "Whiskerbot: A Robotic Active Touch System Modeled on the Rat Whisker Sensory System," *Adaptive Behavior*, vol. 15, no. 3, pp. 223–240, 2007.
- [6] D. Kim and R. Möller, "Biomimetic whiskers for shape recognition," *Robotics and Autonomous Systems*, vol. 55, no. 3, pp. 229–243, 2007.
- [7] C. Tuna, J. H. Solomon, D. L. Jones, and M. J. Hartmann, "Object shape recognition with artificial whiskers using tomographic reconstruction," in *IEEE International Conference on Acoustics, Speech and Signal Processing (ICASSP)*, pp. 2537–2540, 2012.
- [8] C. Will, J. Steigenberger, and C. Behn, "Object Contour Reconstruction using Bio-inspired Sensors," in *Proceedings 11th International Conference on Informatics in Control, Automation and Robotics (ICINCO 2014)*, September 2014, Vienna (Austria), IEEE, pp. 459–467, ISBN: 978-989-758-039-0, 2014.
- [9] G. Dehnhardt, "Tactile size discrimination by a California sea lion (*Zalophus californianus*) using its mystacial vibrissae," *Journal of Comparative Physiology A*, vol. 175, no. 6, pp. 791–800, 1994.
- [10] G. Dehnhardt and A. Kaminski, "Sensitivity of the mystacial vibrissae of harbour seals for size differences of actively touched objects," *The Journal of Experimental Biology*, vol. 198, pp. 2317–2323, 1995.
- [11] G. Dehnhardt, B. Mauck, and H. Bleckman, "Seal whiskers detect water movements," *Nature*, vol. 394, pp. 235–236, 1998.
- [12] M. Schmidt et al., "Technical, non-visual characterization of substrate contact using carpal vibrissae as a biological model: an overview," in *Proceedings of 58th International Scientific Colloquium – Shaping the future by engineering*, September 2014, Ilmenau (Germany).
- [13] M. Brecht, B. Preilowski, and M.M. Merzenich, "Functional architecture of the mystacial vibrissae," *Behavioural Brain Research*, vol. 84, pp. 81–97, 1997.
- [14] G.E. Carvell and D.J. Simons, "Biometric analyses of vibrissal tactile discrimination in the rat," *The Journal of Neuroscience*, vol. 10, no. 8, pp. 2638–2648, 1990.
- [15] Y.S.W. Yu et al., "Whiskers aid anemotaxis in rats," *Science Advances*, vol. 2, no. 8, e1600716, 2016.
- [16] S.Y. Long, "Hair-nibbling and whisker-trimming as indicators of social hierarchy in mice," *Animal Behaviour*, vol. 20, no. 1, pp. 10–12, 1972.
- [17] D. Voges et al., "Structural characterisation of the whisker system of the rat," *IEEE Sensors Journal*, vol. 12, no. 2, pp. 332–339, 2012.
- [18] J. Dörfel, "The musculature of the mystacial vibrissae of the white mouse," *Journal of Anatomy*, vol. 135, no. 1, pp. 147–154, 1982.

- [19] S. Ebara et al., "Similarities and differences in the innervation of mystacial vibrissal follicle-sinus complexes in the rat and cat: A confocal microscopic study," *The Journal of Comparative Neurology*, vol. 449, no. 2, pp. 103-119, 2002.
- [20] K. Carl et al., "Characterization of Static Properties of Rats Whisker System," *IEEE Sensors Journals*, vol. 12, no. 2, pp. 340-349, 2012.
- [21] R.B. Towal et al., "The Morphology of the Rat Vibrissal Array: A Model for Quantifying Spatiotemporal Patterns of Whisker-Object Contact," *PLoS Computational Biology*, vol. 7, no. 4, pp. 1-17, e1001120, 2011.
- [22] A. Ahl, "The role of vibrissae in behavior: A status review," *Veterinary Research Communications*, vol. 10, pp. 245-268, 1986.
- [23] B.W. Quist and M.J.Z. Hartmann, "Mechanical signals at the base of a rat vibrissa: the effect of intrinsic vibrissa curvature and implications for tactile exploration," *Journal of Neurophysiology*, vol. 107, pp. 2298-2312, 2012.
- [24] C. Will, J. Steigenberger, and C. Behn, "Quasi-static object scanning using technical vibrissae," in: Proceedings 58. International Colloquium Ilmenau (IWK), September 0812, 2014, Ilmenau, Germany. ilmedia, URL: <http://nbn-resolving.org/urn:nbn:de:gbv:ilm1-2014iwk:3> [accessed: 2016-06-10], 2014.
- [25] C. Will, J. Steigenberger, and C. Behn, "Bio-inspired Technical Vibrissae for Quasi-static Profile Scanning," Springer International Publishing Switzerland, J. Filipe et al. (eds.), ISBN: 978-3-319-26453-0, pp. 277-295, 2016.
- [26] M. Knutsen, D. Derdikman, and E. Ahissar, "Tracking Whisker and Head Movements in Unrestrained Behaving Rodents," *Journal of Neurophysiology*, vol. 93, pp. 2294-2301, 2004.
- [27] M. Knutsen, A. Biess, and E. Ahissar, "Vibrissal Kinematics in 3D: Tight Coupling of Azimuth, Elevation, and Torsion across Different Whisking Modes," *Neuron*, vol. 59, pp. 35-42, 2008.
- [28] N.G. Clack et al., "Automated Tracking of Whiskers in Videos of Head Fixed Rodents," *PLoS Computational Biology*, vol. 8, no. 7, e1002591, pp. 1-8, 2012.
- [29] S.A. Hires, L. Pammer, K. Svoboda, and D. Golomb, "Tapered whiskers are required for active tactile sensation," *eLife*, 2013, e01350, pp. 1-19, 2013.
- [30] L. Pammer et al., "The mechanical variables underlying object localization along the axis of the whisker," *The Journal of Neuroscience*, vol. 33, no. 16, pp. 6726-6741, 2013.
- [31] G. Scholz and C. Rahn, "Profile Sensing With an Actuated Whisker," *IEEE Transactions on Robotics and Automation*, vol. 20, pp. 124-127, 2004.
- [32] P. Gummert and K.-A. Reckling, "Mechanik (Mechanics)," 3rd edition, Vieweg, Braunschweig, Germany, 1994.
- [33] A. Öchsner and M. Merkel, "One-Dimensional Finite Elements – An Introduction to the FE Method," Springer, Berlin, 2013.